The Influence of the Computational Mesh on the Prediction of Vortex Interactions about a Generic Missile Airframe

Erdem Dikbaş[1]

Defense Industries Research and Development Institute (TÜBİTAK SAGE), Mamak, 06261, Ankara, Turkey

Christian Schnepf[2]

DLR, German Aerospace Center, Göttingen, 37073, Germany

Michael Anderson[3]

Corvid Technologies, Mooresville, NC 28117, USA

Magnus Tormalm[4]

Swedish Defence Research Agency (FOI), SE-164 90 Stockholm, Sweden

Scott Shaw[5]

MBDA UK Ltd, Filton, Bristol, BS347QW, UK

James DeSpirito[6]

U.S. Army Combat Capabilities Development Center – Army Research Laboratory (ARL), Aberdeen Proving Ground, MD 21005, USA

Gaëtan Loupy[7]

MBDA-FRANCE, Le Plessis-Robinson, 92350, France

George Barakos[8] and Kiril Boychev[9]

University of Glasgow, G128QQ Glasgow, UK

Chris Toomer[10]

University of the West of England, Bristol, BS161QY, UK

Özgür Uğraş Baran[11]

Middle East Technical University, Çankaya, 06800, Ankara, Turkey

A research program has been underway for four years to study vortex interaction aerodynamics that are relevant to military air vehicle performance. The program has been conducted under the auspices of the NATO Science and Technology Organization (STO), Applied Vehicle Technology (AVT) panel by a Task Group with the identification of AVT-316. The Missile Facet of this group has concentrated their work on the vortical flow field around a generic missile airframe and its prediction via computational methods. This paper focuses on mesh-related effects and RANS simulations. Simulated vortex characteristics

[1] Senior Researcher, Aerodynamics Division.
[2] Research Scientist, AIAA Member.
[3] Computational Analyst, AIAA Member.
[4] Deputy Research Director, Department of Aerospace Engineering.
[5] Senior Principal Aerodynamicist.
[6] Aerospace Engineer, FCDD-RLW-WD, AIAA Associate Fellow.
[7] Aerodynamic Engineer.
[8] Professor, CFD Laboratory, School of Engineering.
[9] PhD, CFD Laboratory, School of Engineering.
[10] Associate Professor, Department of Engineering Design and Mathematics, Member AIAA.
[11] Assistant Professor, Department of Mechanical Engineering

were found to depend strongly on the properties of the employed mesh, in terms of both resolution and topology. Predictions of missile aerodynamic coefficients show a great dependence on mesh properties as they are sensitive to computed vortex dynamics. Key suggestions about the desired mesh characteristics have been made. Based on these, a shared mesh was constructed to perform common analyses between the AVT-316 Missile Facet members. Mesh based uncertainties of the aerodynamic coefficient predictions were estimated via Richardson Extrapolation method.

I.Nomenclature

C_x, C_y, C_z = aerodynamic force coefficients
C_l, C_m, C_n = aerodynamic moment coefficients
d_{ref} ,D = reference diameter
l, m, n = aerodynamic moment components
p_0 = total pressure
p_∞ = free stream static pressure
$p_{0,\infty}$ = free stream total pressure
q_∞ = free stream dynamic pressure
S_{ref} = reference area, $\pi d_{ref}^2/4$
T_∞ = free stream static temperature
u, v, w = components of velocity vector w.r.t. flow
$|V|$ = magnitude of velocity vector w.r.t. flow
X , Y, Z = aerodynamic force components
μ, μ_t = molecular and turbulent viscosities
σ, λ = incidence and roll angles of the missile

DoF = Degree of Freedom
GCI = Grid Convergence Index
EARSM = Explicit Algebraic Reynolds Stress Model
RANS = Reynolds Averaged Navier-Stokes
RSM = Reynolds Stress Model
SRS = Scale Resolving Simulations
SST = Shear Stress Transport

Variables in Richardson Extrapolation:
c = convergence check parameter
p = order of convergence
r = mesh refinement ratio

II. Introduction

Vortex development on missile bodies has been an active research topic since 1970s. Early research focused on asymmetric vortex shedding, which causes out-of-plane side force in high angle of attack conditions [1-5]. The angular limits of this behavior were analyzed by several researchers [5, 6-8]. Cummings et al. collated these studies and visualized the three angle of attack regimes, which are characterized as symmetric vortices, asymmetric vortices, and vortex wake [9]. Even the problem happens to be in symmetric vortex regime, it is also apparent that vortex development on missile body is also effective in aerodynamic characteristics of downstream components, the results of which can be severe [10].

In January 2018, the NATO Science and Technology Organization (STO) Applied Vehicle Technology (AVT) panel established a Task Group identified as AVT-316 (Vortex Interaction Effects Relevant to Military Air Vehicle Performance). The Task Group was split into two facets: an Aircraft Facet and a Missile Facet, each focusing on the vortex interactions associated with airframes of direct interest to NATO. The Missile Facet was established to (i) Assess the current capabilities of CFD to predict missile aerodynamic characteristics for flows containing multiple vortex interactions; (ii) Share and seek to learn from comparable experience of applying CFD to other classes of NATO vehicles (combat aircraft, in particular); and (iii) Consolidate lessons learned and any attendant future requirements [11]. This paper is one of a series being presented at this conference to provide a technical overview of the activities and accomplishments of the AVT-316 Missile Facet [12-22]. The work is still ongoing: a final output, constituting a more detailed and consolidated technical record, will be published by NATO STO towards the end of 2022.

The first computational results of AVT-316 Missile Facet activity were shown in AVT-307 Separated Flow Symposium, which took place in Trondheim, Norway in October 2019 [11]. Computational results available up to that date provided a good means for commencing remarks about OTC1 test case in terms of flow topology and sensitivity of the results against numerical methods and modeling choices as well as computational mesh. Initial studies indicated the effect of how well the upstream vortex interactions are resolved, on rolling moment generated by the tail fins. One of the most conspicuous findings was the difficulty in reaching mesh independence for rolling moment coefficient, although up to a few hundreds of millions degree of freedom meshes were employed. Apart from that, maximization of number of cells with hexahedral topology was shown to be an important factor to attain a less dissipative character in computed vortex dynamics.

In this paper, influence of the computational mesh on the OTC1 test case results is extensively discussed with a focus on RANS simulations. Firstly, OTC1 test case is described in the next part. Initial meshes part covers a cumulative description of meshes produced by each partner during their own mesh independence study. In this part, influences of mesh resolution and cell topology on flow field predictions are discussed. Advanced meshes section highlights the benefits of more sophisticated approaches in mesh creation. Overall, these discussions provide the basis towards the adoption of the 'shared' mesh, which almost every partner has utilized in their solvers. Mesh convergence analysis contains investigations with both statistical and systematic approaches. In the statistical (overview) part, results of more than 400 RANS analysis submitted by partners are evaluated. Systematic mesh convergence study covers Richardson Extrapolation analysis with dedicated set of each of unstructured mesh and structured grid.

III.Test Case Definition

The AVT-316 Missile Facet initially performed computations on OTC1 missile geometry, which is essentially composed of a slender body, low-aspect-ratio and slender wings in the middle and stability/control fins at tail. The outer mold line had been produced by MBDA UK and was shared to the Facet members in common formats at the start of the activity. Several geometric features are shown in the Fig. 1. The body starts with an ogive nose having ten millimeter tip radius and continues as a long cylinder up to the base. Wing and fin sets are attached to the body in cross (✕) configuration. Cross section profiles of constant-chord-length wings are in hexagonal shape, whereas fins are lofted by double-wedge root and tip profiles.

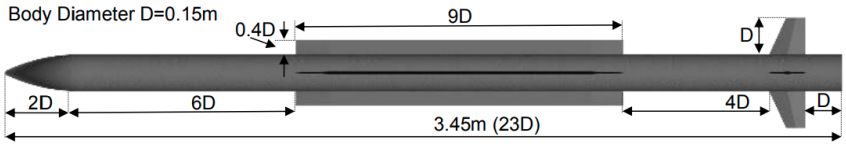

Fig. 1 The generic OTC1 missile geometry.

In this paper, flow and aerodynamic quantities are expressed in body-fixed North East Down (NED) coordinate system, where x, y and z-axes point forward, starboard and downward directions, respectively. Origin of the coordinate system is fixed to the nose tip. Velocity vector orientation with respect to body coordinate system is described by total incidence –sometimes referred to as total angle of attack- (σ) and roll angle (λ). Total incidence is defined as the angle between body x-axis and velocity vector of missile. Roll angle is the angle between the projection of velocity vector on yz-plane and z-axis. Positive direction is described as counter clockwise when looked from rear by convention. Roll angle can simply be set by positive rotation of missile about x-axis after the total incidence orientation is set. It is also possible to set up the velocity vector without any rotation of the geometry, using following relations: $u=|V|\cos(\sigma)$, $v=|V|\sin(\sigma)\sin(\lambda)$, $w=|V|\sin(\sigma)\cos(\lambda)$. Wings and fins are numbered from one to four starting from the one in starboard bottom direction and increasing in clockwise direction when looked from rear.

The flow condition of primary interest is selected as Mach 1.4, total incidence angle $\sigma = 15°$ and roll angle $\lambda = 2.5°$. Previous work points that, in this particular flow arrangement, variance of aerodynamic coefficient results between different computational setups is higher [11]. Also, the specified flow Mach number can be considered as a typical value for the maneuvering speeds of supersonic missiles. Static thermodynamic properties of the free stream air is taken from sea-level standard conditions (p_∞ = 101325.0 Pa, T_∞ = 288.15 K). Throughout the paper, aerodynamic force and moments are expressed as coefficients, defined as $C_{X,Y,Z} = (X,Y,Z)/(q_\infty S_{ref})$ and $C_{l,m,n} = (l,m,n)/(q_\infty S_{ref} d_{ref})$, where X,Y,Z,l,m,n are aerodynamic forces and moments in respective body axis directions, q_∞ is the freestream dynamic pressure, d_{ref} is diameter of body cylinder, and S_{ref} is cross-sectional area of the body cylinder.

For the initial exploratory study performed by AVT-316, partners were instructed to adopt their favored practices and standards for creation of the initial OTC1 test case meshes. Each partner generated multiple computational meshes on the test case geometry using his or her tools of choice, which resulted in different meshing styles, mesh sizes, and software utilized in the mesh creation. For example, some partners chose to utilize the symmetry of the geometry, while others modeled the entire geometry. This inherently created a wide variety of initial meshes for the OTC1 test case.

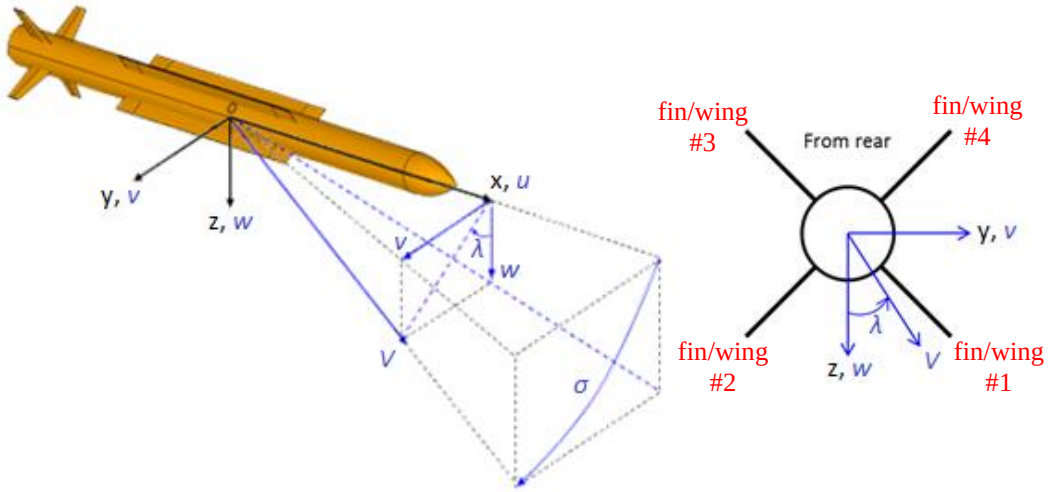

Fig. 2 Coordinate system and definitions.

IV. Initial Meshes

Initial meshes were produced by each partner who committed to perform mesh dependency analysis. At this stage, participants made use of their own tooling and best practices. For this reason, resultant meshes were with dissimilar topology and size distributions. The primary target of this stage for participants was to get familiarized with the physical and numerical aspects of the OTC1 test case. Furthermore, it yielded a good opportunity to establish necessary ground for communication and common language while sharing results. A wide variety of commercial and in-house meshing and solution tools were utilized, as listed in Table 1.

Table 1 Meshing and solver tools used at the initial mesh studies

ORGANIZATION	Mesh Generation Software	Flow Solver
Corvid Technologies	Pointwise [23]	RavenCFD [24]
DLR	CENTAUR [25]	TAU [26]
FOI	ICEMCFD [27] (surface) / TRITET [27] (volume)	M-Edge [29]
MBDA F	ANSA [30]	FLUSEPA [31]
MBDA UK	SOLAR [32]	TAU [26]
TÜBİTAK SAGE	ANSYS [33] (surface) / TGRID [34] (volume)	FLUENT [35]
University of Glasgow	ICEMCFD [27]	HMB3 [36]
ARL	CAPSTONE [37]	CFD++ [38] / KESTREL [39]

A. Construction and Properties

For the initial mesh refinement study, each partner was encouraged to create meshes with coarse, medium, and fine levels of resolution for the OTC1 test case in order to analyze mesh convergence for their family of meshes. Some partners took further steps with refinement, creating additional extra and superfine meshes to further explore results and convergence. Each level of mesh resolution was achieved through a systematic method of refinement. However, due to the nature of unstructured meshes and their variability, a true family of meshes cannot be achieved with unstructured meshes. An example of systematic surface refinement with unstructured meshes is shown in Fig. 3 by Corvid Technologies, where the surface cell edge lengths were cut in half for each level of refinement.

This refinement on the surface is then translated into the volume mesh through the prismatic cell growth from the surface, along with a density in the nearfield controlling the maximum cell size in which a cell edge length can grow. Fig. 4 shows the resulting coarse, medium, and fine volume meshes that correspond to the surface meshes displayed in Figure 1. Larger prismatic growth can be observed on the coarse mesh as a result of the larger surface cell edge lengths. This is due to the prismatic growth using an aspect ratio between the surface edge length and the height of the last layer for the cut off of the prismatic growth.

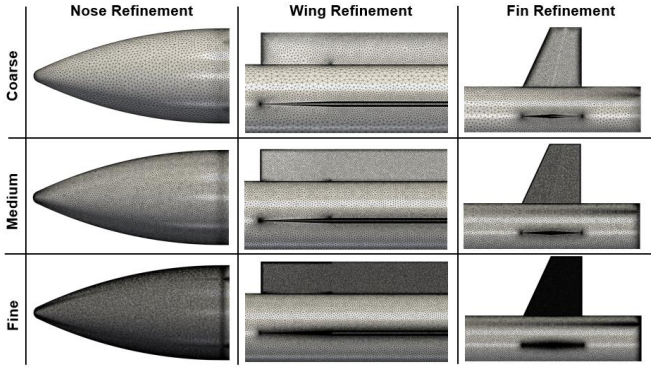

Fig. 3 Example of coarse, medium, and fine levels of surface mesh refinement along the nose, wing and fin regions by Corvid Technologies on the OTC1 test case.

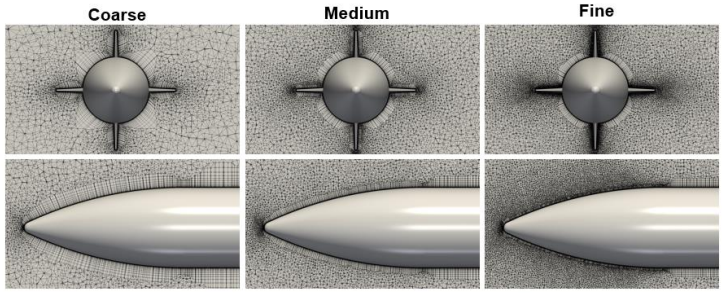

Fig. 4 Volume mesh for coarse, medium, and fine levels of mesh refinement for the surface meshes displayed in Fig. 3.

Due to different methodologies being used by partners during the mesh creation process, a method of tracking mesh similarity and key mesh metrics was adopted. The method of tracking the meshes was in the form of a spreadsheet in which each partner submitted their key mesh metrics for each of the meshes that they created. For the surface mesh, the key mesh metrics that were recorded are displayed in Fig. 5, in which average cell edge lengths along these key areas were recorded. Similarly, key metrics in the volume region of the mesh were also recorded including the density and wake refinement region (shown in Fig**.** 6), overall domain size, and prismatic growth parameters.

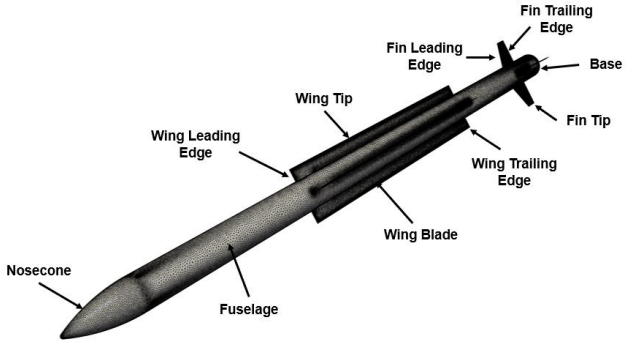

Fig. 5 Key areas along the surface of OTC1 test case in which average cell edge length values were tracked for each mesh created.

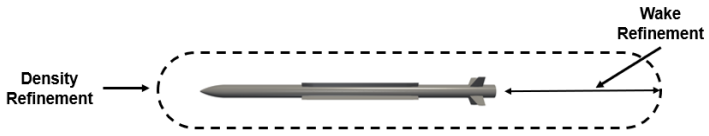

Fig. 6 Density and wake refinement regions recorded in the key mesh metrics spreadsheet, including size and cell edge length of both the density and wake refinement areas.

Using the recorded data of surface and volume mesh metrics for each partner's family of meshes, a collection of important surface mesh metrics is visualized in Fig. 7. In this figure, bars represent the cell edge length value reported for each partner's medium mesh, with the error bars indicating the variation between the coarsest and finest meshes. For example, looking at ARL's nose cone sizing shows 4mm edge length used for the medium mesh, while the coarsest mesh utilizes 8 mm and the finest using 3 mm. Already evident in this figure is the large distribution of cell edge lengths used by each partner for each of the various mesh refinement levels. It should be noted that due to the variety of solvers used by all partners, the appropriate metric for number of degrees of freedom (DoF) for each mesh was selected. For example, with cell-centered codes the number of cells in the mesh was selected for the DoF, while vertex-based codes used number of nodes in the mesh for their DoF. Overall, the coarsest mesh was 4 million DoF, while the finest of the initial meshes consisted of 428.9 million DoF.

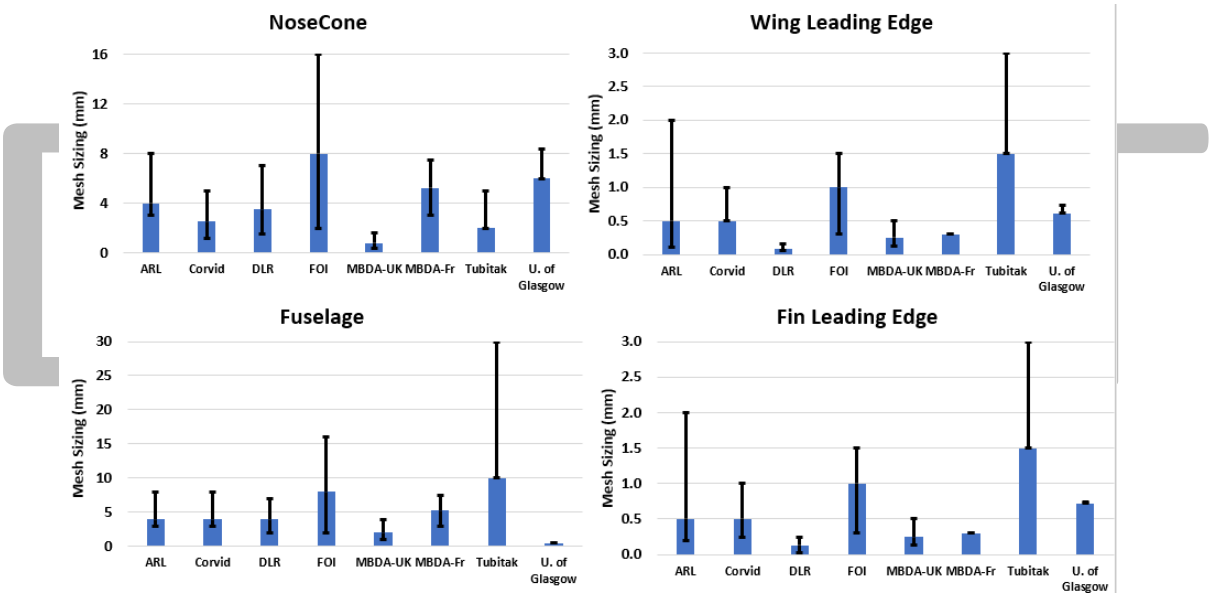

Fig. 7 Variation in surface sizes for initial meshes created by each partner. Bars represent the surface sizes reported for each partner's medium mesh, with error bars representing the spread in surface sizes between the coarsest and finest meshes.

Additionally, common views of each partner's medium used in this initial exploratory study are shown below in Fig. 8. In this figure, top row displays the overview of the volume mesh in the nearfield of the missile geometry using a slice through the centerline at y=0. Second row highlights a crucial area of the flow at the junction of the leading edge of wing 4 and the body of the missile. Third row displays a volume slice through x = -1.21 m along the surface of wing 1. Finally, bottom row shows the volume mesh using a slice through the fins at x = -3.225 m with the surface mesh being displayed for the base region. Overall, the variation between each partner's standard practices varies and consequently can be observed in these images.

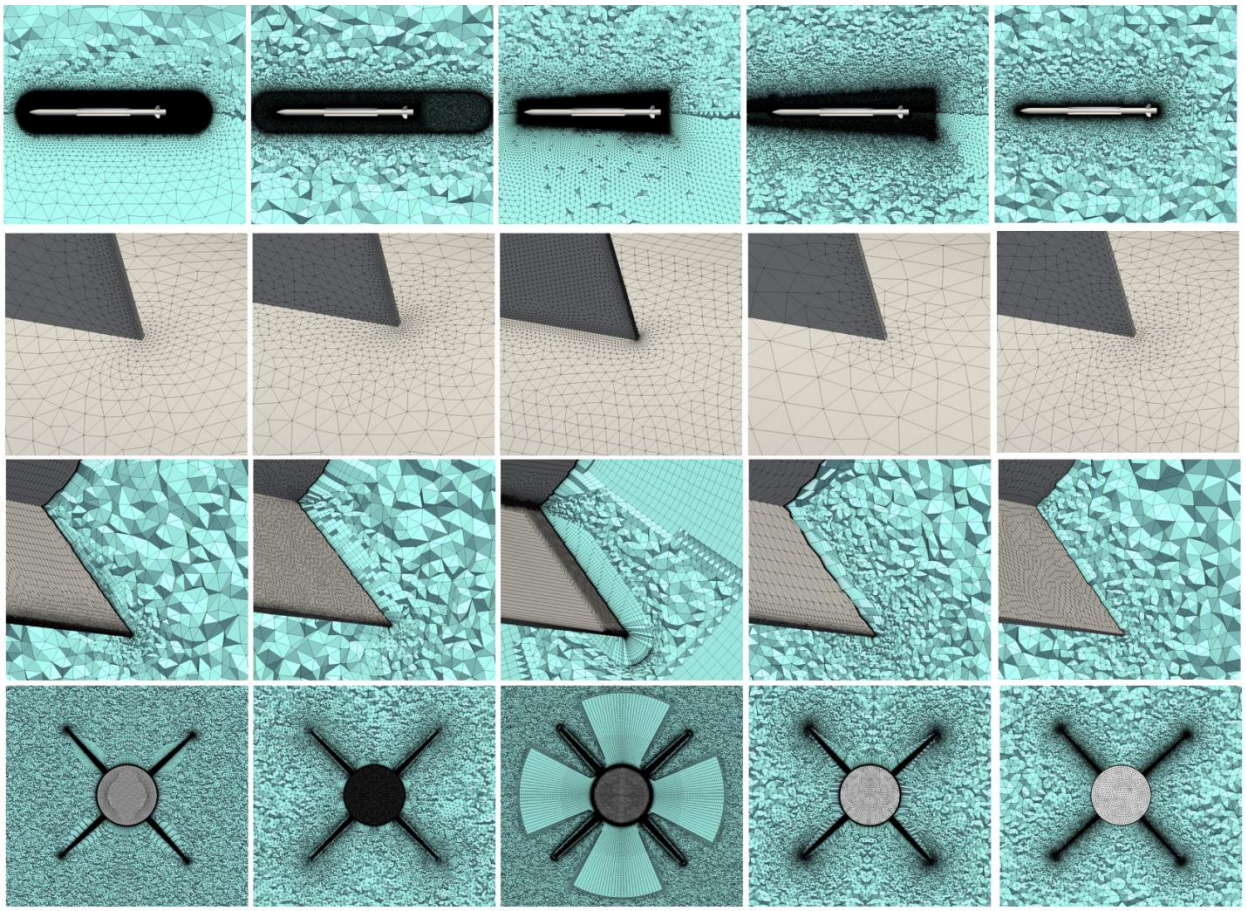

Fig. 8 Views of medium meshes generated by each partner from left to right column: i. ARL, ii. Corvid Technologies, iii. DLR, iv. FOI, v. TÜBİTAK SAGE.

B. Results & Discussion

1. *Influence of mesh resolution*

Once initial meshes were created, partners ran the mandatory flow conditions using the numerical and algorithm settings of their choice. Fig. 9 shows the integrated forces and moments in the body reference frame for the full missile as a result of these simulations. In this image, the x-axis is plotted with number of degrees of freedom. As previously mentioned, the DoF metric was appropriately selected based on whether the solver used was cell-centered or vertex-based. What can be immediately observed from this figure is the large spread in missile integrated forces and moments. Normal force and pitching moment show datasets trending toward convergence beyond 100+ million DoF, but none appear to fully reach convergence. Rolling moment shows one of the largest distributions in data with over a 100% spread from the mean value. It should be noted that the SAS simulations predict over double the value that RANS calculations predict. This has been investigated further using other scale resolving methods in the analysis of the OTC1 test case, which is discussed in the separate paper focusing particularly to utilization of hybrid RANS/LES methods [16]. Overall, mesh convergence is not shown to be achieved in any of the forces and moments or family of meshes. This has been investigated through various techniques including additional mesh refinement, both manual (see Part V) and automated (see Ref. [13]), and Richardson analysis (see Part VI).

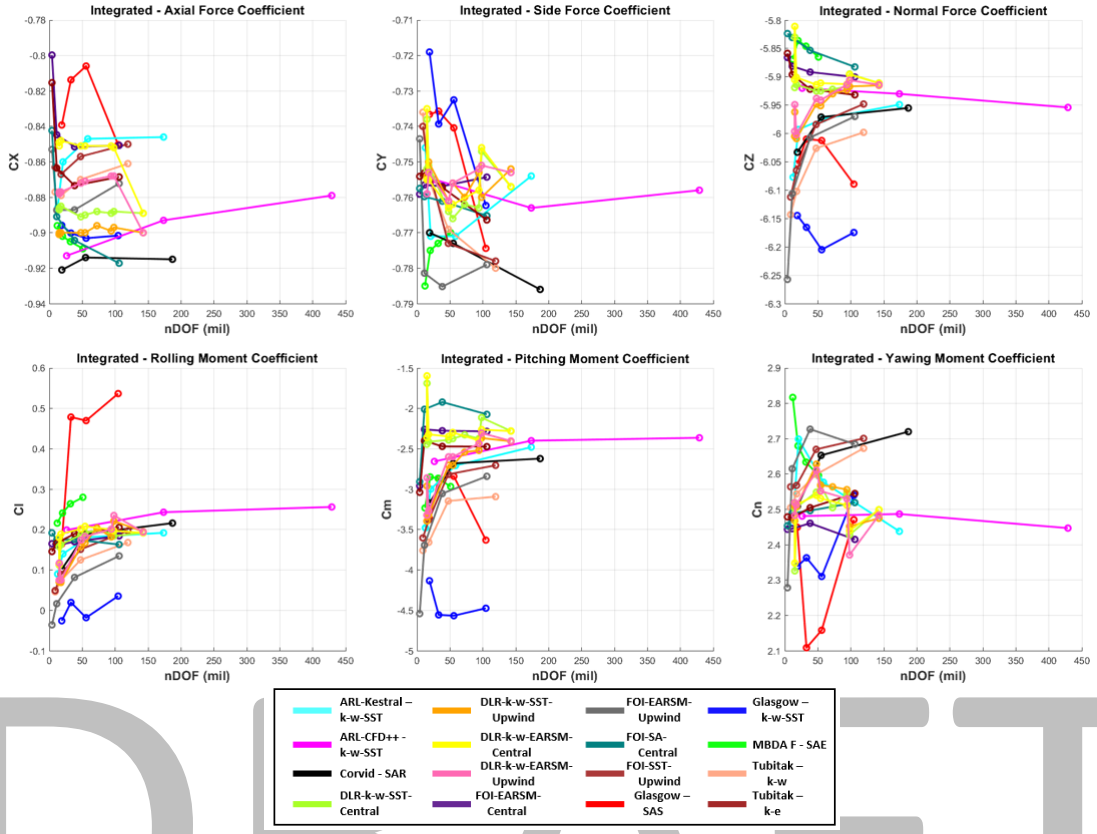

Fig. 9 Results from initial mesh study from all partners with various turbulence models and numerical settings, showing integrated forces and moments on OTC1 geometry. X-axis displays degrees of freedom (in million) of the mesh used indicating higher mesh resolution when moving from left to right.

2. *Influence of cell topology*

Initial meshes constitute a wide variety of mesh topologies from unstructured hybrid tetrahedral grid to full hexahedral Cartesian grids. These meshes are composed of cell elements with several cell topologies which may coexist in a selected example of mesh used in whole activity. In the common hybrid mesh generation approach, surface mesh is typically inflated towards the flow domain, so prismatic elements take place in the vicinity of the wall. Remaining region up to the domain extents is filled with either of tetrahedral, hexahedral and polyhedral cells or their desired combinations. In the OTC-1 problem, vortical flow features are observed outside of the prismatic cells. Therefore, the assessments provided in this section focus on the topological effects of the volume filling elements.

Influence of cell topology on the computed flow fields of vortex flow problems is essentially associated with the amount of the numerical dissipative character of the individual cell shapes. Tetrahedral elements are known to be more dissipative compared to hexahedral ones but they are frequently preferred for its relatively effortless application on complex three-dimensional geometries. On the contrary, hexahedral mesh generation, usually being applied with a block structured sense, requires more complicated user intervention. The two dimensional counterparts of these element types have also been investigated in the numerical dissipation context linked with limiter effects in Ref. [14]. In that paper, superiority of structured quadrilateral elements over unstructured triangular elements on accuracy of gradient calculation is explicitly shown on the two-dimensional isentropic vortex case.

At the very early stages of computational work on the OTC1 test case of the AVT-316 activity, DLR conducted RANS simulations to investigate the influence of cell topology by means of comparisons between so-called type-A and type-B. The type-A is the class of the common unstructured tetrahedral meshes, while the latter class indicates the extended hexahedral layers into various zones between wings and fins in order to maximize the benefits of the hexahedral elements. The mesh type selection shows significant effect in overall rolling moment coefficient of the OTC1, as illustrated in Fig. 10. Computed total pressure fields show that vortex preservation is the most important feature that drives rolling moment predictions. Fig. 11 shows that utilization of hexahedral elements provides better

preservation of vortices down to fin section, which can be considered as analogous to two-dimensional isentropic vortex case results in Ref. [14].

As seen in Fig. 11, core locations of vortices are also affected by cell topology used in the mesh and they move inboard and upward when type B mesh is utilized. These deviations are possibly due to vortex-vortex interactions resolving capability, as the individual vortex paths are subject to be influenced by neighboring vortex structures. For instance, employment of hexahedral elements enables to observe a different vortex structure at fin section with additional cores, which might be one of the reasons for more upward and inward computed locations of the vortices acting on fins number 3 and 4. Similar observations have been made by Corvid Technologies with their RavenCFD code. In addition to unstructured hybrid and type-B grids, they have supported their investigation with addition of an overset grid with structured hexahedral elements effective in the vortex interaction zone. Meshes making use of hexahedral cell topology have yielded substantially better preserved vortex predictions and higher rolling moment coefficients. These common observations can be considered as valid regardless of employed turbulence model, as DLR used Reynolds Stress Model (RSM) while Corvid used Spalart-Allmaras with rotation correction (SAR) as turbulence models.

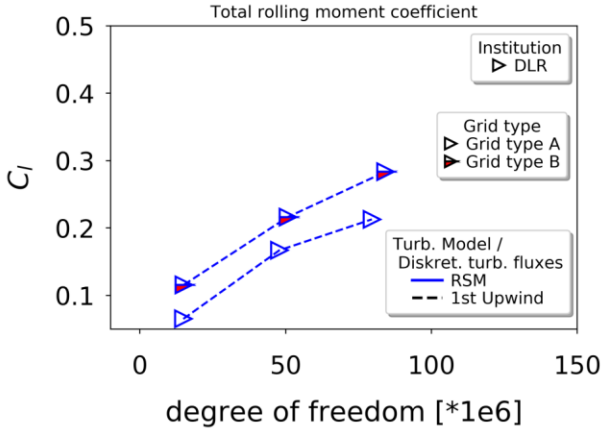

Fig. 10 Total rolling moment coefficient comparison between type-A (hybrid unstructured) and type-B mesh results; DLR, Tau, RSM, upwind scheme

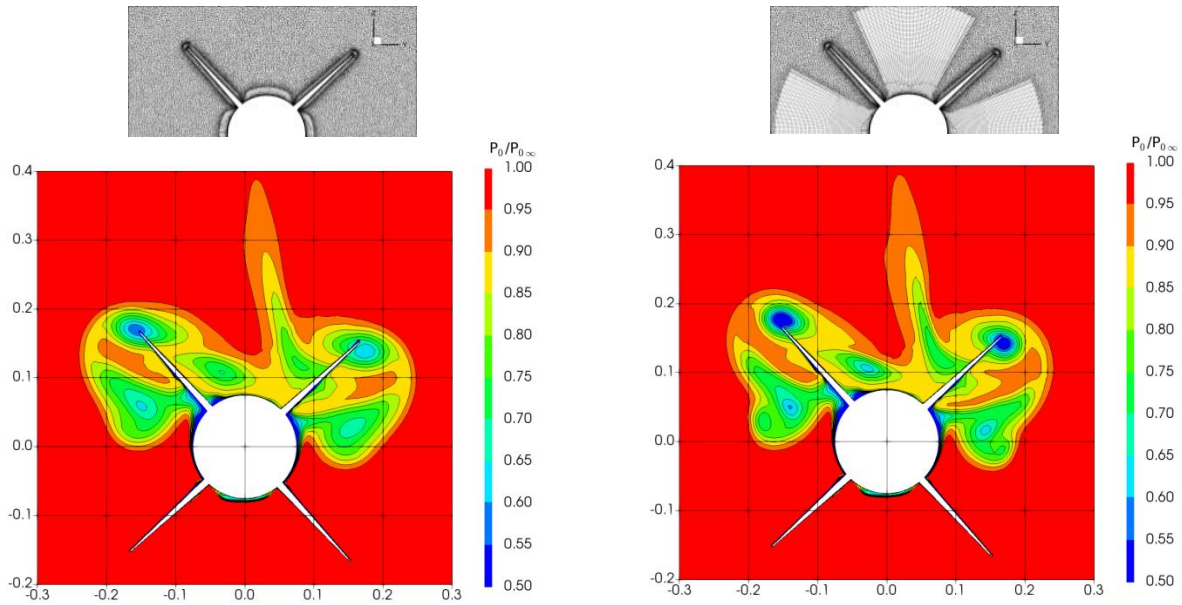

Fig. 11 Total pressure contours at fin mid-chord section (x/D=-21.5); left: unstructured tetrahedral, right: type B hexahedral, additional vortex core marked; DLR, Tau, RSM, fine mesh, upwind scheme. TODO: figures to be replaced with new format

Polyhedral mesh is another cell type investigated in this report, making use of surface and volume elements with arbitrary topology. Application of polyhedral meshes on complex geometries is usually as effortless as of unstructured tetrahedral mesh; indeed a common approach to generate polyhedral mesh elements is to perform through conversion from a tetrahedral element pattern. The converting principle is to adopt nodes of source triangular (or tetrahedral) mesh as polyhedral cell centers, and centers of neighboring edges and cells of source mesh node as polyhedral cell nodes. Despite its convenience for automatization, only a few solvers support this type of elements at the moment. Indeed, during the activity, the only organization who performed computations with polyhedral mesh is TÜBİTAK SAGE with use of commercial Fluent code.

Overall rolling moment results of TÜBİTAK SAGE computations show a great variation with respect not only to element size but also to cell topology. Fig. 12 illustrates that influence of cell topology is intensely dependent on the gradient calculation scheme but not on turbulence model employed. Tetrahedral mesh with Green-Gauss cell based gradient calculation results are very far from overall converging trend even with 120 million-element mesh. However, use of polyhedral mesh diminishes the disadvantage of Green-Gauss cell based gradient method, which in general requires lower computational resources than the node based method. Cross plane plots at fin section explicitly show that higher rolling moment predictions are obtained when vortices impinging on upper fins are better preserved (Fig. 13, column [i] vs. columns [ii, ii, iv]). It is also observable that, although it might be partly responsible of slight changes in vortex core locations, eddy viscosity ratio prediction (at the presented range) does not influence the computed core total pressure deficit. Therefore, the influence of cell topology is directly as a result of convective discretization error, rather than being an indirect effect that prediction of any of turbulent variable causes.

Results collected in the initial meshes phase have provided a strong insight about required meshing properties when vortex interactions play important role on aerodynamics of generic missile airframe. It is worth here to recall the major findings reached within this stage. Firstly, the degree of freedom should be at least in the order of 100 million to accomplish credible fixed-mesh RANS solutions for OTC1 test case. In this regard, Automatic Mesh Refinement (AMR) can be suggested as a favorable method to reduce the computational loads. Secondly, use of cell topologies other than tetrahedral significantly improves the vortical flow field characteristics. Using structured hexahedral elements at least for the critical regions of the flow may be advisable considering its superiority in numerical properties and supportability amongst flow solvers.

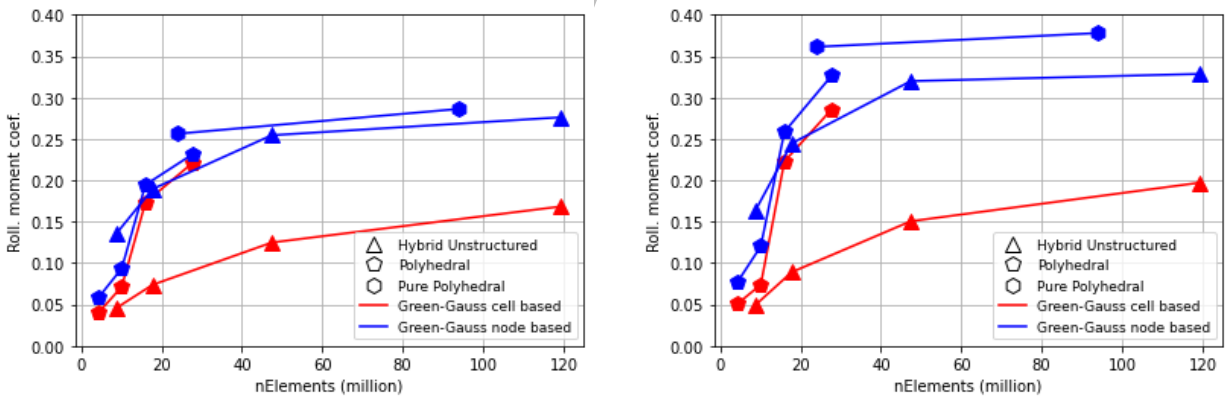

Fig. 12 Grid resolution effects on rolling moment coefficients for different cell topologies and gradient calculation methods; left: SST, right: Realizable k-ε; TÜBİTAK SAGE, Fluent, 2nd order upwind scheme.

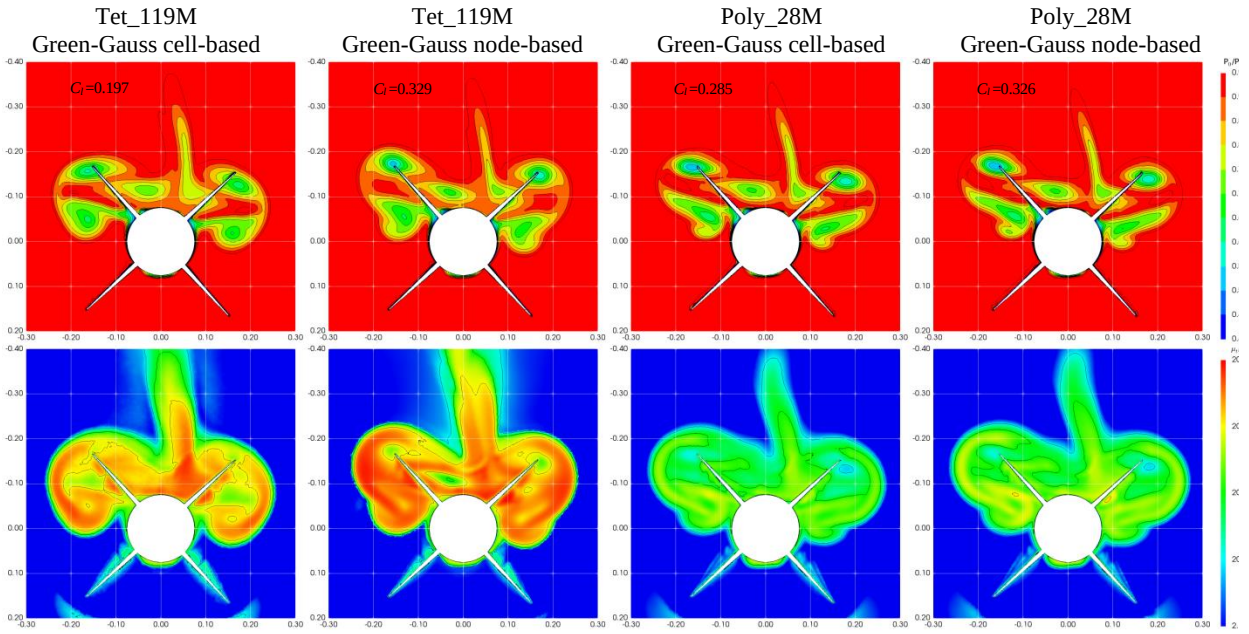

Fig. 13 Total pressure (top row) and eddy viscosity ratio (bottom row) contours at fin mid-chord station (x/D=-21.5, TÜBİTAK SAGE, Fluent, Realizable k-ε, 2nd order upwind scheme.

V. Advanced Meshes

Initial mesh studies showed that the flow solution for the OTC1 test case is strongly dependent on mesh resolution and cell element topology used. Missile aerodynamic coefficients, especially rolling moment, are influenced by the vortex field prediction around the missile geometry. Apart from this, it was also observed by AVT-316 Missile Facet members that other aspects of a computational setup -such as choices of discretization schemes, limiters, turbulence modeling- causes significant variations in the flow field predictions [14]. At this point there arose a need for dissociation of these multiple effects on the different aspects of predicted flow field characteristics. For this purpose, more focused studies were planned for RANS [15] and Scale Resolving Simulations (SRS) [16]. As widely known, computational requirements for SRS is still substantial so the physical time required for this type of analyses would be much weightier. In order to proceed with a time-effective strategy from this point, AVT-316 Missile Facet members decided to use a 'shared mesh', which was not only to reduce the effort spent on meshing but also to eliminate the mesh-dependent differences between the future simulations.

In the 'advanced meshes' part, we present the basis and benefits of manually refined meshes based on the experience gathered during initial mesh studies. As an important outcome, a common mesh was generated and shared to other partners by DLR, though FOI also made a great contribution to advanced mesh studies. The product mesh has been used in computations conducted by various partners.

A. Construction

As in the present case, an unstructured hybrid grid approach is commonly the first choice to discretize complex geometries. In contrast to a fully structured grid, the computational mesh generation is generally simpler for unstructured grids. In addition, a finer resolution of certain areas in the grid can be easily limited locally. However, also structured grids have advantages. In preliminary investigations they have been shown not only for the OTC1 test case but also for a generic vortex a lower numerical dissipation [14]. Another advantage is the better control of the element size, which is favorable with regard to grid convergence studies and the generation of a grid family. The alignment of the grid to the flow characteristics and the skewness of elements can also be better controlled with structured grids in most cases. This reduces discretization errors [40, 41]. Furthermore, as reported in Ref. [41] they are more suitable to prevent a grid induced flow asymmetry. Finally, a well-designed computational mesh with hexahedral elements has fewer elements as a comparable unstructured mesh.

Hybrid unstructured grids combine the advantages of structured grids with those of unstructured grids by using a "quasi-structured" grid for the discretization of the boundary layer. For the OTC1 test case, DLR adopted to utilize a different approach where the structured layers are extended to near field (Fig. 14). Therefore, the boundary layer

mesh on the cylindrical body of the missile already consists largely of hexahedra. This mesh is than extended in wall normal direction to achieve the so-called Type B mesh type. Only near the wing and rudder junctions hexahedrons have not been used. Here a clustering of grid nodes exists to resolve the leading and trailing edges well. If a fully structured approach had been chosen, this clustering would have affected the entire structured part of the grid and increase the mesh size significantly. In this part of the geometry, prismatic elements were used instead. A more detailed description of the grid topology of the Type B mesh for the OTC1 test case can be found in chapter 3. In general, the rule of thumb for a mesh like Type B is that hexahedra should be used for as many surface areas as possible. This simply increases the area in which the structured mesh can be extended in the wall normal direction.

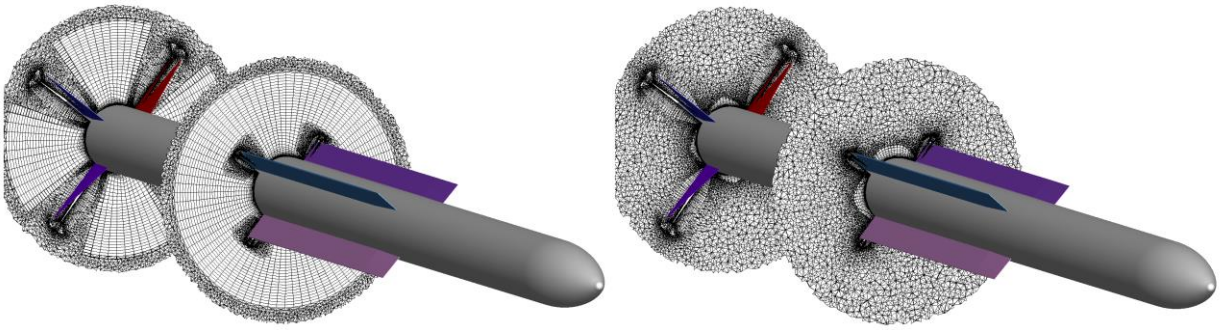

Fig. 14 Comparison of the Type B mesh approach of DLR (left) with a common hybrid grid (right).

For the generation of the computational meshes of DLR the Centaur Software [25] was used. The approach for the surface mesh was the same for all different mesh sizes and mesh types in this study. An attempt was made to mesh the surface as far as possible in a structured manner with square elements. Classical triangular elements were used only in the areas where this approach would lead to clustering. Therefore, the regions with unstructured triangular elements are determined as following: (i) the nose, (ii) leading/trailing edges of the wings, (iii) fin surfaces, and (iv) junction zones between wings/fins and body. Fig. 15 shows the partition of the surface mesh into unstructured and structured element zones, colored in grey and green, respectively. Resulting surface mesh in different sections at medium resolution level is shown in Fig. 16. This surface mesh topology was used then to generate the boundary layer mesh. Boundary layer mesh was generated by applying a procedure similar as in classical approach in hybrid unstructured meshing. As a distinctive feature of the Type B approach, the structured part of the boundary layer mesh was extended in wall normal direction. The extent of the structured area is shown as green blocks in Fig. 17 for test case OTC1.

Fig. 15 Partition of the surface mesh into area with rectangular elements (green) and triangular elements (grey).

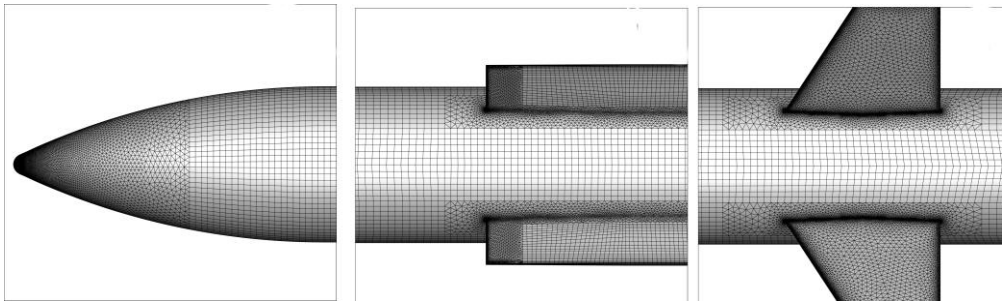

Fig. 16 Medium surface mesh of different missile sections of the OTC1 test case (nose-, wing-, fin section).

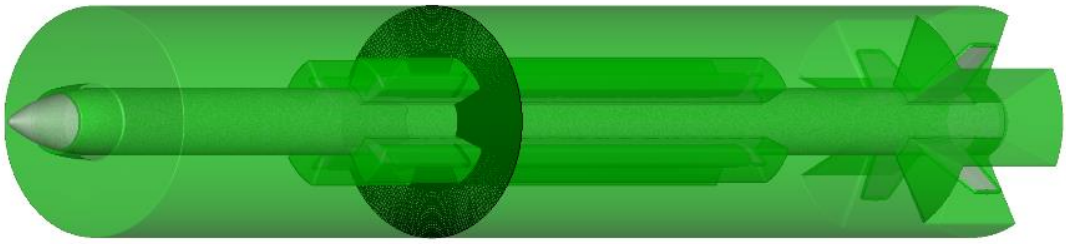

Fig. 17 Mesh topology of the Type B mesh for the OTC1 test case.

FOI also accomplished to generate an advanced mesh set using commercial meshing tool Pointwise [23]. The first Pointwise mesh layout, the fine, was setup similar to the DLR common topology but without the lower quadrant hex domain and with the structured domains increased compared to the common mesh. The structured wedge shaped volume extended to the same outer radii from the nose to the fin trailing edge. The unstructured tetrahedral parts are connected to the structured blocks using voxel elements. For the second Pointwise mesh, the ultrafine, the density was refined to improve scale resolving simulations. The tip of the nose was dominated by triangular elements instead of quads. Furthermore, the radial extend of the structured blocks were optimized with a smaller radius at the forward part as well as an increase in circumferential extent to reduce the gap containing tetrahedral elements.

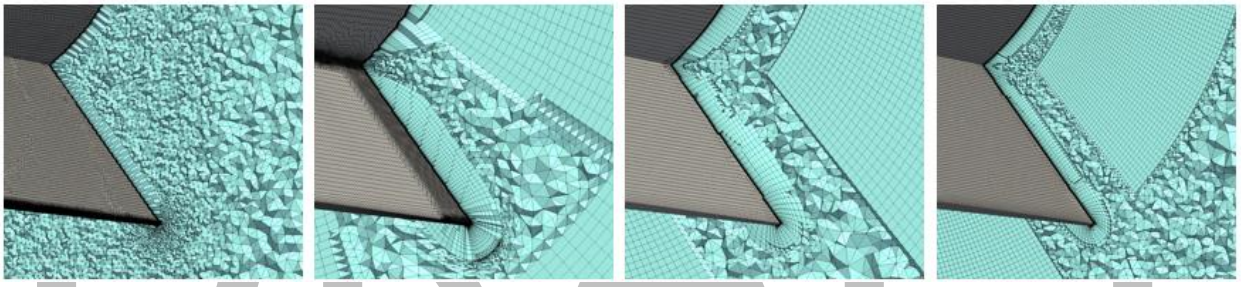

a. FOI-OTC1-ULT b. DLR-OTC1-COM c. FOI-OTC1-PWF d. FOI-OTC1-PWU

Fig. 18 Cross sectional view of advanced meshes generated by FOI (-c- and -d-, being fine and ultrafine, respectively), in comparison with unstructured ultrafine mesh (a) and medium Type B mesh generated by DLR (b).

Surface, volume and boundary layer sizing properties of the advanced meshes are listed in Table 2. Total number of cells ranges between 37.4 and 434.4 million, whereas minimum and maximum numbers of nodes are 15.1 and 209.5 million. Between the same-level meshes generated by either partner, DLR meshes are finer in majority of surfaces and FOI meshes are finer in the density box. Properties of shared mesh are a combination of properties of both fine meshes. Majority of surface mesh characteristics are similar from the DLR Fine mesh, whereas boundary layer and volume mesh characteristics are taken from the FOI Fine mesh. Detailed explanations about the development of the shared mesh will be provided after the results section, since choices made while developing the shared mesh are based on those results presented in the next section.

Table 2 Properties of advanced meshes (lengths given in millimeters)

		DLR					FOI	
	Component	**Coarse**	**Medium**	**Fine**	**Ultra**	**Shared**	**Fine**	**Ultra**
Surface	Nosecone	max. 7.0	3.50	3.00	1.50	1.00	1.30	1.00
	Fuselage	7.00	4.00	3.00	2.00	2.50	1.30	1.00
	Wing Leading Edge	0.16	0.08	0.08	0.05	0.08	1.0/0.33	1.0/0.33
	Wing Trailing Edge	0.16	0.08	0.08	0.05	0.08	1.0/0.33	1./0.33
	Wing Tip	0.16	0.08	0.08	0.05	0.08	2.1/1.0	1.00
	Wing Blade	6.00	3.00	1.80	1.50	1.80	2.0/1.5	1.00
	Tail Leading Edge	0.25	0.13	0.13	0.03	0.13	1.5/0.33	1.0/0.33
	Tail Trailing Edge	0.25	0.13	0.13	0.03	0.13	1.5/0.33	1.0/0.33
	Tail Tip	0.25	0.13	0.13	0.03	0.13	1.00	0.5/1.0
	Tail Panel	5.00	2.50	1.40	1.00	1.40	1.50	0.7/1.0
	Base	3.00	2.00	2.00	2.00	2.00	1.30	0.85
Boundary Layer	First Layer Height	0.001	0.001	0.001	0.001	0.001	0.001	0.001
	Prism/Hex Growth Ratio	1.25	1.2	1.15	1.15	1.19	1.2	1.2
	Max Number of Prisms	40	46	54	54	46	45	45
Volume	Density box	12.0	6.00	4.00	1.0/ 4.0	2.00	3.5/2.5	1.0
	Total Cells [M]	37.4	131.6	280.4	434.4	240	94.2	347.8
	Total Nodes [M]	15.1	50.7	98.0	209.5	84	51.8	186.8

B. Results & Discussion

Advanced meshes were used by several participants in their computations. This gave an opportunity for preliminary cumulative analysis as total number of submissions is over 150, compared to over 250 submissions in the initial mesh phase. It has already been shown that the rolling moment coefficient (Cl) is a useful integral quantity which indicates how well the vortices and their interactions are resolved. Distribution of rolling moment coefficients and their linear regressions with respect to degree of freedom for each mesh group is shown in Fig. 19 (left). This figure illustrates that the Cl coefficient shows a large scatter for the advanced mesh group, which is similar to previously presented initial mesh results. Also, computed rolling moment coefficient has an increasing trend with increasing grid resolution. The mean computed Cl is higher when advanced meshes are utilized. Primary advantage of using advanced meshes is that the higher Cl values, i.e. better preserved computed vortices, can be achieved with less number of degree of freedom. Secondly, as right hand side sub-figure of Fig. 19 suggests, advanced meshes yields to a converging trend in the Cl, whereas the initial mesh results keep linearly increasing trend up to the finest mesh level.

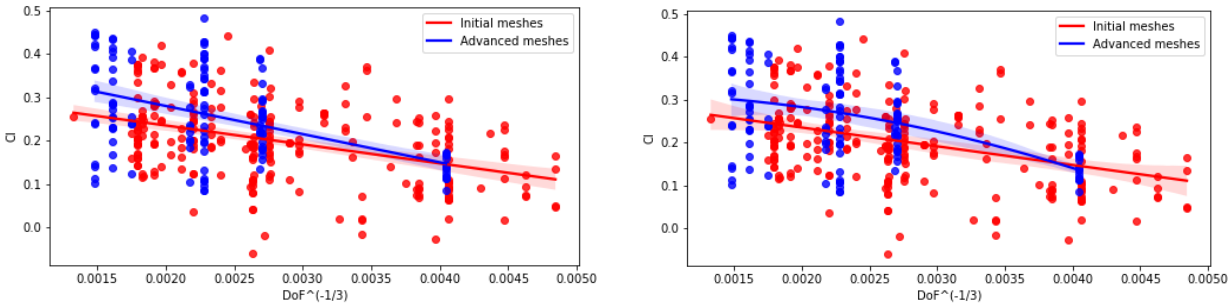

Fig. 19 Rolling moment coefficient distributions and their first (left) and second (right) order regressions with respect to average cell size (Smaller x-axis values implies denser mesh.).

After the cumulative analysis, we investigate the mesh effects for more specific computational setups. Fig. 20 shows the rolling moment coefficients calculated with the advanced mesh approach. For comparison, the coefficients found with conventional hybrid meshes are also shown. For the upwind method, the Cl values computed with the advanced mesh are always larger than those computed with a hybrid mesh with a similar number of DoF regardless of the flow solver and the turbulence model used. In the case of **Central scheme, no general trend can be observed. For the medium and fine level meshes (DoF less than 125 million), a similar behavior as for the**

upwind upwind scheme is observable. However, this is no longer the case with the very coarse and superfine meshes. In Fig. 21 **the total pressure and helicity distributions in two different cross sections are shown. For all investigated turbulence models, the flow field visualization for the Type-B mesh on equal sized meshes shows more details and concentrated vortex cores as the standard hybrid meshes. The flow field visualization for the Type-B mesh shows a more detailed flow topology and more concentrated vortex cores than the standard hybrid mesh with a similar size. This finding is confirmed by figures showing the helicity in cross-section. For the Type-B mesh, the primary vortices show larger helicity values than the corresponding vortices of the hybrid mesh. These observations are independent of the discretization scheme and the turbulence models investigated.**

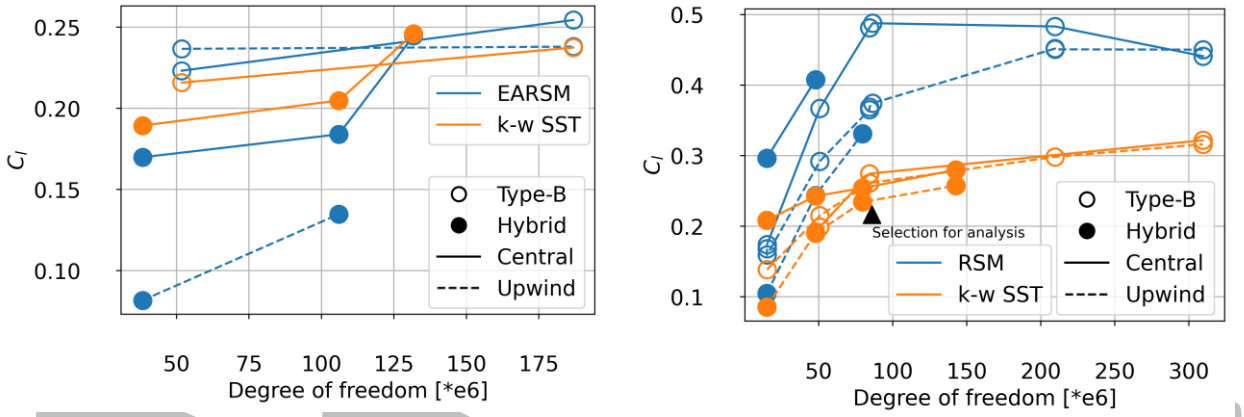

Fig. 20 Influence of the Type-B mesh on the rolling moment (left: FOI, M-Edge, right: DLR, TAU-Code).

Type-B, x/D=-12.5 Hybrid, x/D=-12.5 Type-B, x/D=-21.5 Hybrid, x/D=-21.5

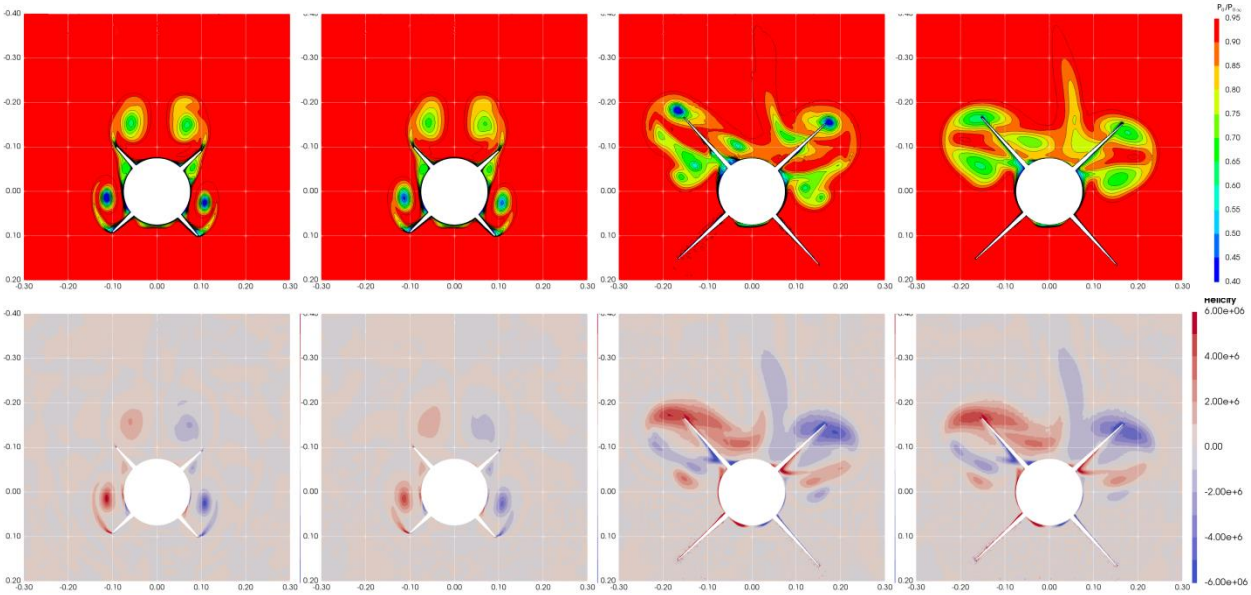

Fig. 21 Total pressure (top row) and helicity (bottom row) distributions showing the influence of Type-B mesh topology; DLR, TAU, RSM, upwind.

The major distinctions of FOI meshes compared to DLR counterparts are wider structured blocks in tangential direction and finer cells in those structured blocks. On the other hand, surface spacing of the DLR mesh is much finer. The finer resolution within structured volume helps to preserve better the vortex shed from the bottom wings, as illustrated in Fig. 22. Larger elements in DLR fine mesh trigger numerically more dissipated flow field. Similarly, the shear layers at the tips of the bottom wings severely dissipate in the computations with DLR fine mesh, as a consequence of larger tetrahedral zone around the wings. Another important observation is that the computed vortex

core locations are significantly different in spite of the cross section location relatively close to the point that the bottom wing tip vortices originate. The mesh resolution in structured volume may again be effective on vortex core location. However, vortex path may also be influenced by the surface mesh sizing of the wings. Fig. 23 depicts the effect of surface mesh sizing on the vortex separation line. Computation with DLR fine mesh provides less diffused flow field in the vortex separation region.

DLR Fine Mesh FOI Fine Mesh

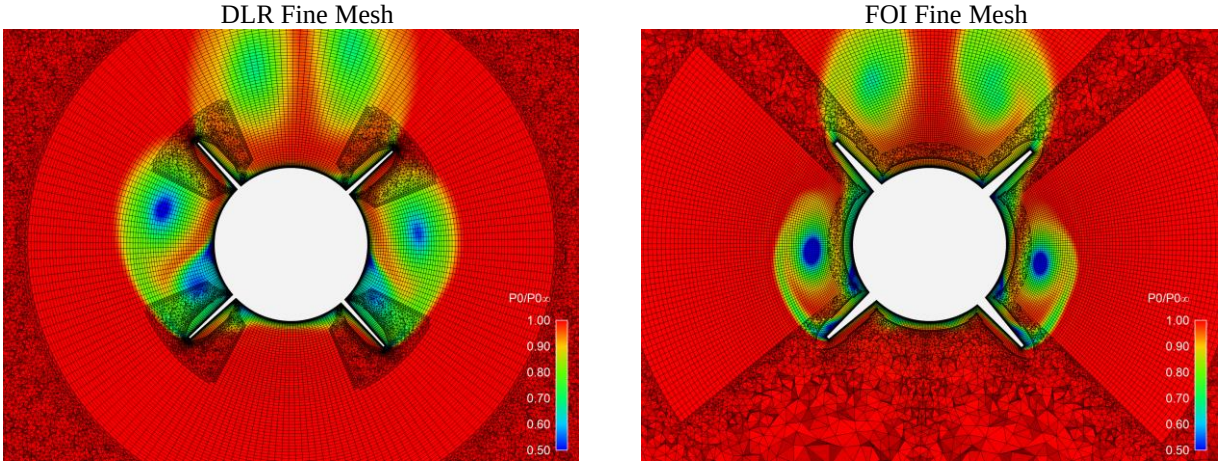

Fig. 22 Influence of increasing tangential extents and reduced element size of structured blocks on total pressure distribution at x/D=-13.3, FOI, M-Edge, RANS, EARSM.

DLR Fine Mesh FOI Fine Mesh

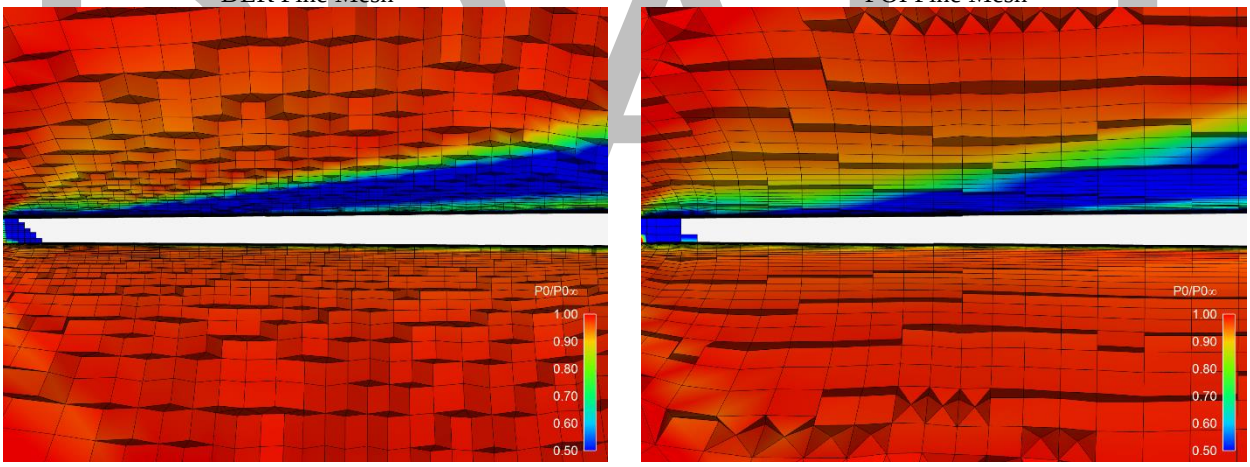

Fig. 23 Influence of surface mesh size on wing surface on total pressure distribution longitudinal plane perpendicular to wing 1 direction, FOI, M-Edge, RANS, EARSM.

C. Shared Mesh Development

Discussions through the computations with manually refined advanced meshes led to the determination of the properties of the shared mesh. The Type-B mesh topology which DLR suggested provided significant benefits on the vortex preservation performance of a RANS computation. FOI pointed out the locational improvements so that better resolved vortex characteristics were achieved. Superior properties of meshes generated by either partner were combined as guided by the advanced mesh results and their discussion.

The common mesh was generated and shared by DLR to other partners for their computations. Simulations with different flow solvers for the common computational mesh were carried out as part of the OTC1 test case. A mesh with the Type-B topology was selected for this purpose. This type of grid showed superior properties than a common hybrid unstructured grid for the current investigation. A mesh size was chosen that was suitable for all participants to undertake RANS simulations but also SRS. Discussion on adequacy of the shared mesh for SRS is in the scope of another paper presented in this special session [16]. The most important mesh metrics are shown in Table 3.

Table 3 Metrics of shared mesh

Parameter	Designation	Value	Figure
Number of nodes	-	84 million	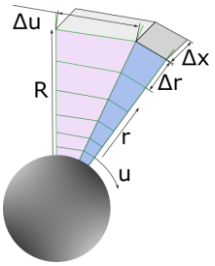
Number. of elements	-	240 million	
Elements in circumferential direction	$2\pi R/\overline{\Delta u}$	188	
Number of structured layers	$R/\overline{\Delta r}$	109	
Edge length in x-direction	$\overline{\Delta x}$	2.5 mm	
Outer radius of hexahedron block	R	262 mm	
Radius of density box	-	250 mm (Nose tip)/ 450 mm (Rear)	
Max. (tetra) cell size within refined area	-	4 mm	

The full 3D mesh was built from a two times mirrored quarter mesh generated with Centaur (Figure3). Since different flow solvers (CFD++, DLR TAU-Code, Fluent, Kestrel, M-Edge, Raven CFD) were used and these partly require different mesh formats, the mirrored mesh was converted into different mesh formats such as CGNS, TAU native, SU2 native and CFD++ native file formats. Every partner could download the appropriate file format from Google Drive. Although a common mesh was used in a certain phase of the study, it is important to bear in mind when analyzing the data that the resultant finite volumes are not identical as both node-centered (M-Edge and Tau) and cell-centered (others) flow solvers were utilized. The discussion of computational results within the common mesh study is not in the scope of this paper. They are comparatively discussed with a focus on modeling effects in another paper of the current AVT-316 special session [15].

VI. Mesh Convergence Analysis

Mesh convergence analysis with regard to OTC1 test case is composed of two parts. At first, it was aimed to understand which aerodynamic coefficient is more sensitive to the mesh resolution. In this part, available RANS coefficient data submitted by all partners were used as inputs for the regression analysis. Secondly, Richardson Extrapolation procedure was applied using the data generated during the participants' own mesh convergence study in the initial mesh phase. The input datasets for the convergence analysis were generated using both unstructured and structured meshes. Each partner applied refinements on the meshes based on their own best practices, so there were no definite common rules or instructions followed. Richardson Extrapolation was applied to the six overall aerodynamic coefficients.

A. Overview

In this section, a statistical analysis of the whole aerodynamic coefficient data submitted by all authors was carried out. Fig. 24 summarizes the counts of the submitted dataset with respect to partners, turbulence model families and non-dimensional average cell length, calculated as DoF^(-1/3). In total nearly 400 submissions were collected. The most frequently used turbulence models were of k-w and SA variants. Vortical corrections of the turbulence models were activated in nearly 30% of the submissions. Distribution of each of these parameters is fairly even. For this reason, it is expected that the regression analysis reflect the grid size dependence correctly.

The sensitivity of each aerodynamic coefficient with respect to average element length is shown in Fig. 25. In this figure, the ranges of y-axes are determined according to the magnitude of the respective coefficient. Amongst the force coefficients (left hand side sub-figure of Fig. 25), Cx appears as the most sensitive coefficient. Nevertheless, it shows a very slight change compared to the moment coefficients. We can conclude that the error caused by possible improper grid sizing is not more than 2% for force coefficients. Sensitivity of moment coefficients are significantly higher, as shown in right hand side sub-figure of Fig. 25. The reason is that the mesh size primarily alters the flow topology effective on tail fins, where a small change in force components creates large deviation on moment components because of the distance. The rolling moment appears as the most influenced parameter by the mesh element size. Table 4 summarizes the properties of regression line of each parameter. Mean regression lines of Cl and Cm deviate from their mid-values by 136% and 25%.

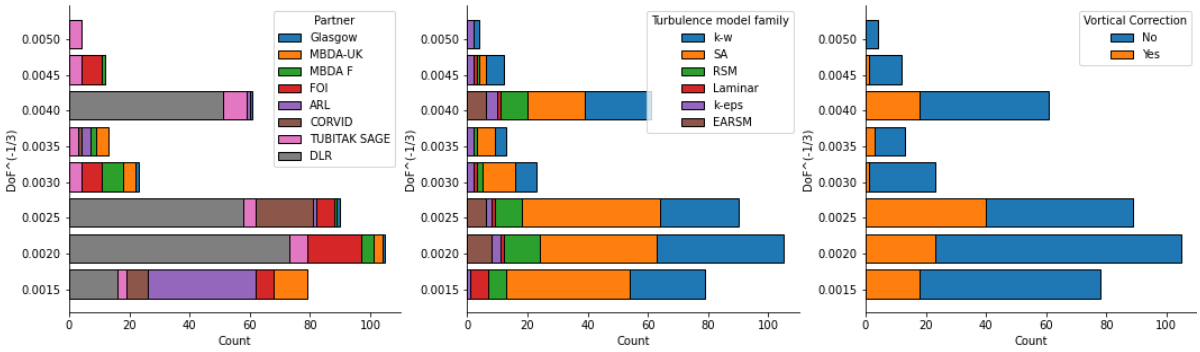

Fig. 24 Distributions of submitted computations with respect to partner, turbulence model family and degree of freedom.

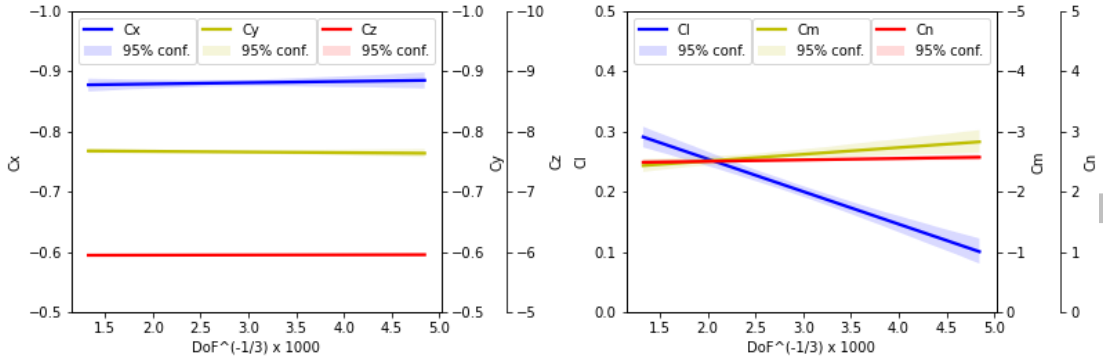

Fig. 25 Linear regression result of each coefficient with respect to average cell length (Smaller x-axis values implies denser mesh.)

Table 4 Regression line statistics

	Cx	Cy	Cz	Cl	Cm	Cn
DoF^(-1/3) = 0.00133	-0.8676	-0.7673	-5.9420	0.2812	-2.3980	2.4942
DoF^(-1/3) = 0.00484	-0.8829	-0.7617	-5.9580	0.0530	-3.0961	2.5697
% deviation from mid-value	1.740	0.735	0.268	136.55	25.41	2.982

B. Richardson Extrapolation

1. *Background information*

In this work, two different approaches have been taken to interpreting the results of the mesh sensitivity investigation. The first is the standard Richardson Extrapolation [42, 43]. Richardson Extrapolation is based on the assumption that the discrete solution has a series representation in the mesh element size. If the formal order of accuracy of the discretization scheme is known then the method provides an estimate of the discretization error when using solutions from two different meshes, a comprehensive treatment can be found in Roache [44]. With the results from two related meshes or grids, Richardson extrapolation gives an estimate of the exact solution:

$$f = f_1 + \frac{f_1 - f_2}{r^p - 1} \tag{1}$$

where f is the estimate of the exact solution, f_1 is the result from the finest mesh, f_2 is the result from the coarser mesh, r is the mesh refinement index and p is the formal order of accuracy of the discretization scheme.

The second approach is Roache's Grid Convergence Index (GCI) [44, 45], which is a development of Richardson extrapolation. The analysis begins with the error metric:

$$E_1 = \frac{f_1 - f_2}{r^p - 1} = \frac{f_1}{r^p - 1}\varepsilon \quad (2)$$

where,

$$\varepsilon = \frac{f_1 - f_2}{f_1} \quad (3)$$

which Roache [44] considers to be better than ε alone since it is an ordered error estimator that properly accounts for the formal order of accuracy of the numerical scheme and the mesh refinement. Based upon these arguments Roache has proposed the use of a grid convergence index (GCI) [45]:

$$GCI = F_s \frac{|\varepsilon|}{r^p - 1} \quad (4)$$

as a systematic way of reporting discretization error. Where asymptotic mesh convergence has been demonstrated a safety factor $F_s = 1.25$ is recommended [46]. For cases in which asymptotic mesh convergence cannot be demonstrated a safety factor of $F_s = 3.0$ is recommended.

2. *Application on initial mesh computations*

Convergence of the aerodynamic coefficients with respect to mesh density was evaluated utilizing Richardson extrapolation method. This study is based on a subset of the results that had been submitted by the partners at the initial observations and mesh convergence analysis stage. Aerodynamic coefficient data set was extracted from the common OTC1 results sheet filled by each partner. The groups for the convergence analysis were formed from three submissions with the same settings except the mesh density. If the number of the submissions with the same settings was more than three, the densest mesh set was selected.

Richardson's extrapolation method was applied to six overall aerodynamic coefficients. Element size was predicted from the total number of elements as follows: h = DoF^(-1/3). Predicted exact result, error band with 95% confidence, order of convergence "p" and convergence check parameter "c" was stored for each coefficient. The quality of the extrapolated value was checked using "p" and "c". Theoretical value for "p" is 2.0, which implies second order convergence. A "p" value less than unity show divergence rather than a convergence. Therefore, the first condition for a valid extrapolation was determined as (p>1). The convergence check parameter is based on Roache's Grid Convergence Index (GCI) and calculated via following formula:

$$c = \frac{GCI_{12}}{GCI_{23} \cdot r^p} \quad (5)$$

where r is the refinement ratio between levels 2-3 and 1-2 [45]. Values between 0.85 and 1.15 were determined as the second indicator of valid extrapolation, since this parameter ensures the asymptotic convergence.

Table 5 presents the valid extrapolations for each aerodynamic coefficient. Although vast majority of the submissions showed convergent trend for each coefficient, nearly half of them have asymptotic character for most of the coefficients. Number of valid extrapolations was found as the lowest for Cn and highest for Cz. It is very difficult to classify the submissions showing better performance in terms of validity of extrapolations. Likewise, there is no correlation found amongst the simulation setups, well-converged coefficients and the orders of convergence. However, computation sets carried out with upwind scheme converge better than those with central scheme in general. The extrapolations showing converging trend (p>1) are plotted in Fig. 26. Those failing in the convergence check are plotted in transparent colors. The coefficient results purified from the mesh dependence are visible on the very left of each subfigure (DoF^(-1/3) = 0).

The mesh size independent results presented in Fig. 26 enabled to evaluate the modeling and numerical scheme effects on the aerodynamic coefficients. For example, Spalart-Allmaras family of models predicted consistently higher magnitude of Cx than the SST turbulence model did. Similarly, laminar computation estimated Cx as -0.62, which is far low in magnitude compared to any prediction with turbulence model. The highest Cl coefficient value was estimated by MBDA-F computation with SA-E turbulence model and central scheme, whereas the lowest value was predicted by MBDA-UK computation with SA-Neg turbulence model. The latter's grid independent result is as low as 0.11. This is probably associated with incapability of SA-Neg turbulence model in resolving vortex flow properties. This drawback is also examined in a more focused paper in this AVT-316 special session [15].

Order of convergence (p) reaches to very high values, on the contrary to the theoretical value second order convergence. While most of the solvers employ second order discretization methods, majority of the valid

extrapolations has p-values higher than 2. This may be associated with use of unstructured meshes, complexity of the flow, non-standard refinement strategies of partners and any other reasons that authors are not aware of. Validated extrapolation results for each aerodynamic coefficient are gathered together in the Appendix. Grid refinement ratio (r), order of convergence (p), and convergence check criterion (c) are provided for each case. Grid independent results of the coefficients are given with their error band within 95% confidence interval (Table 6).

Table 5 Convergence of Richardson extrapolation

Partner	Turb. Model	Sch.*	Mesh Type*	Cx		Cy		Cz		Cl		Cm		Cn	
				p	c	p	c	p	c	p	c	p	c	p	c
Uni. of Glasgow	SST-SAS	U	S-O	7.52	0.05	8.16	0.03	14.4	0.00	12.0	0.00	13.98	0.00	7.56	0.05
Uni. of Glasgow	SST	U	S-O	3.42	1.13	6.42	0.08	1.35	1.13	1.55	1.15	9.40	0.02	6.39	0.08
MBDA-UK	SA-N	C	U-T	4.02	1.01	0.11	0.92	0.50	1.77	8.22	1.11	0.03	3.68	0.13	0.95
MBDA-F	SA-E	C	U-T	0.44	1.00	3.13	0.38	3.75	0.31	2.38	1.06	11.58	0.03	1.20	0.99
FOI	SA	C	U-T	0.50	0.72	4.54	0.05	1.48	0.37	8.66	0.00	1.80	0.27	4.54	0.05
FOI	SST	C	U-T	1.82	0.83	3.36	0.10	1.99	1.00	0.48	1.08	7.91	1.00	1.86	0.29
FOI	Laminar	C	U-T	2.80	0.99	7.48	0.95	0.34	0.84	2.94	1.12	3.96	0.08	13.1	0.99
ARL – CFD++	SST	U	U-T	3.45	0.12	0.98	0.49	8.00	0.00	1.04	1.05	2.46	0.98	2.16	0.03
ARL – Kestrel	SST	U	U-T	6.34	0.99	33.5	1.01	10.1	1.00	3.79	1.30	5.21	0.90	3.00	1.87
CORVID	SAR	U	U-T	4.56	1.09	3.15	0.08	3.91	1.00	3.55	1.14	6.07	0.98	2.41	1.03
TÜBİTAK SAGE	k-e	U	U-T	0.65	0.99	4.53	1.01	2.34	0.99	0.69	1.31	4.89	0.96	3.54	1.01
TÜBİTAK SAGE	SST	U	U-T	0.05	0.99	0.64	1.01	3.03	1.00	0.31	1.35	6.80	0.98	1.18	0.50
TÜBİTAK SAGE	k-e	U	U-P	1.56	0.97	2.13	1.02	10.4	1.00	6.32	1.28	19.67	0.98	16.00	0.00
TÜBİTAK SAGE	SST	U	U-P	2.97	0.99	16.36	1.06	11.5	1.00	5.62	1.28	28.29	1.02	0.71	0.94
DLR	EARSM	C	U-T	4.72	0.31	15.5	0.02	2.10	0.59	9.38	0.67	1.38	0.77	18.63	0.01
DLR	EARSM	U	U-T	2.68	0.58	14.5	1.00	1.79	1.00	4.22	0.54	59.47	0.00	43.4	0.00
DLR	SST	C	U-T	19.64	0.01	7.43	0.16	3.95	0.37	3.49	1.05	5.87	0.25	7.77	0.15
DLR	SST	U	U-T	1.21	0.42	3.36	0.58	2.54	0.58	2.06	0.51	3.74	0.60	3.56	1.01
DLR	SAO	U	U-T	4.75	0.60	36.6	0.00	0.64	0.48	41.1	0.00	78.50	0.00	70.87	0.00
Extrapolations satisfying p>1				15		17		16		15		18		17	
Extrapolations satisfying p>1 and 0.85<c<1.15				7		6		9		6		8		5	

* Scheme → U: Upwind, C: Central; Mesh Type → S: Structured, O: Overset, U: Unstructured, T: Tetrahedral, P: Polyhedral

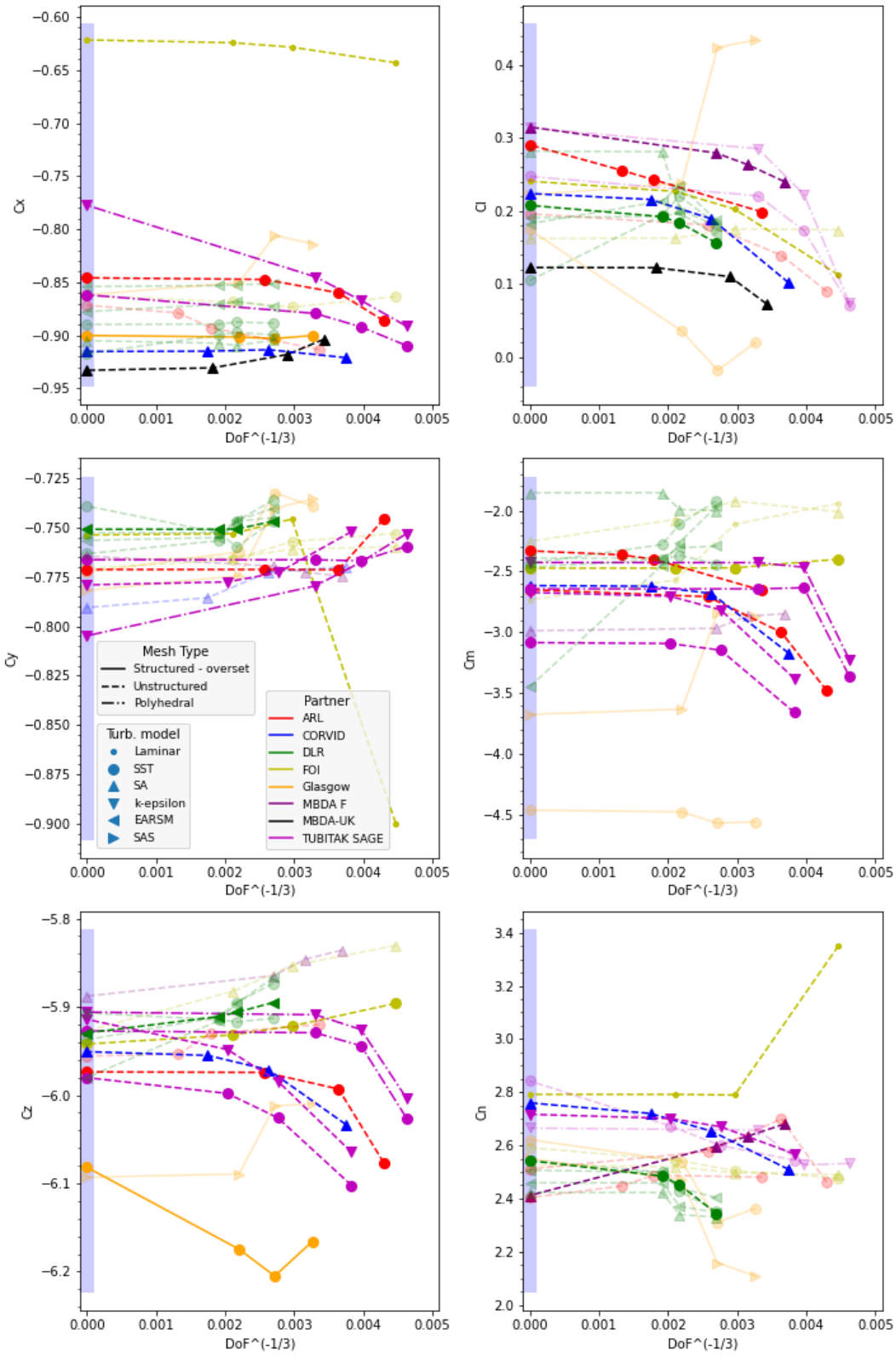

Fig. 26 Richardson extrapolation of initial mesh results. Only converging results (p>1) are plotted. Results failing in convergence check via parameter c are transparent.

VII. Summary & Conclusion

In this paper, we thoroughly discussed the mesh effects on the OTC1 test case of AVT-316 Missile Facet, with a focus on RANS simulations. A broad range of meshes in terms of resolution level, cell type and topology was employed in the flow simulations. Aerodynamic coefficients were strongly influenced by mesh characteristics, as the strengths and paths of the vortices originating from the upstream components disturbed the flow field parameters on tail fin section. It was observed that the most sensitive aerodynamic coefficients are rolling and pitching moments. Higher rolling moment predictions were made as the vortices were better preserved against the numerical dissipation.

For the OTC1 test case, none of the results were shown to be completely mesh independent. Converging trends were observable for meshes with 100+ million degree of freedom, which may still be a challenging requirement for today's computer technology, considering total number of flow conditions required to be simulated for a typical missile airframe. Adaptive mesh refinement would potentially be an effective tool to get rid of global reduction in element sizes. Further studies are required to establish best practices focusing on AMR.

Hexahedral and polyhedral element types show superior vortex preservation, compared to tetrahedral elements, which are widely used in off-body zones of external aerodynamic flow applications. Polyhedral cells are not supported by most of the solvers but they may still be preferable for applicable solvers. Application of hexahedral cells can be achieved via overset or extended layer (Type-B) mesh topologies. In current study, manual mesh refinement based on Type-B topology provided a considerable improvement in the resultant flow field predictions. Similarly, manually refined meshes showed significantly better mesh convergence characteristics.

Mesh convergence analysis via Richardson Extrapolation method exhibited very irregular results. None of the submissions could achieve well-converged extrapolations for all six aerodynamic coefficients. However, some of the submissions showed good convergence for a number of individual aerodynamic coefficients. The orders of convergence are fairly higher than the theoretical second order convergence for most of the well-converged submissions. Possible reasons for these irregularities in the convergence behaviors are significant dependence on the dissipation of the solver (employed scheme), turbulence model used, and the type of mesh. Despite these ambiguities, a set of mesh independent coefficient results could be obtained. For most of these results, uncertainty values within 95% confidence are reasonable. On the other hand, exact coefficient values, especially for rolling moment, show large scatter, which addresses the strong dependence on modeling and numerical effects.

Appendix

Table 6 Richardson extrapolation results

Group #	Partner	Turb. Model	Sch.*	Mesh Type*	r	p	c	exact value	lower bound	upper bound
Cx										
2	Glasgow	SST	U	S-O	1.23	3.42	1.13	-0.900	-0.903	-0.900
3	MBDA-UK	SA-N	C	U-T	1.59	4.02	1.01	-0.933	-0.934	-0.928
7	FOI	Laminar	C	U-T	1.40	2.80	0.99	-0.622	-0.628	-0.621
9	ARL	SST	U	U-T	1.41	6.34	0.99	-0.846	-0.849	-0.845
10	CORVID	SAR	U	U-T	1.50	4.56	1.09	-0.915	-0.915	-0.915
13	TÜBİTAK SAGE	k-e	U	U-P	1.20	1.56	0.97	-0.777	-0.929	-0.761
14	TÜBİTAK SAGE	SST	U	U-P	1.20	2.97	0.99	-0.862	-0.901	-0.857
Cy										
7	FOI	Laminar	C	U-T	1.40	7.48	0.95	-0.754	-0.754	-0.752
9	ARL	SST	U	U-T	1.41	33.49	1.01	-0.771	-0.771	-0.771
11	TÜBİTAK SAGE	k-e	U	U-T	1.36	4.53	1.01	-0.779	-0.779	-0.776
13	TÜBİTAK SAGE	k-e	U	U-P	1.20	2.13	1.02	-0.805	-0.811	-0.748
14	TÜBİTAK SAGE	SST	U	U-P	1.20	16.36	1.06	-0.766	-0.766	-0.766
16	DLR	EARSM	U	U-T	1.13	14.53	1.00	-0.751	-0.751	-0.751
Cz										
2	Glasgow	SST	U	S-O	1.23	1.35	1.13	-6.082	-6.291	-6.059
6	FOI	SST	C	U-T	1.40	1.99	1.00	-5.942	-5.945	-5.919
9	ARL	SST	U	U-T	1.41	10.09	1.00	-5.974	-5.975	-5.974
10	CORVID	SAR	U	U-T	1.50	3.91	1.00	-5.951	-5.96	-5.950
11	TÜBİTAK SAGE	k-e	U	U-T	1.36	2.34	0.99	-5.914	-5.991	-5.906
12	TÜBİTAK SAGE	SST	U	U-T	1.36	3.03	1.00	-5.980	-6.02	-5.976
13	TÜBİTAK SAGE	k-e	U	U-P	1.20	10.41	1.00	-5.906	-5.913	-5.905
14	TÜBİTAK SAGE	SST	U	U-P	1.20	11.52	1.00	-5.927	-5.932	-5.927
16	DLR	EARSM	U	U-T	1.13	1.79	1.00	-5.930	-5.934	-5.888
Cl										
3	MBDA-UK	SA-N	C	U-T	1.59	8.22	1.11	0.123	0.122	0.123
4	MBDA F	SA-E	C	U-T	1.17	2.38	1.06	0.315	0.235	0.324
7	FOI	Laminar	C	U-T	1.40	2.94	1.12	0.241	0.209	0.245
8	ARL	SST	U	U-T	1.35	1.04	1.05	0.291	0.212	0.300
10	CORVID	SAR	U	U-T	1.50	3.55	1.14	0.224	0.206	0.226
17	DLR	SST	C	U-T	1.13	3.49	1.05	0.208	0.173	0.212

Group #	Partner	Turb. Model	Sch.*	Mesh Type*	r	p	c	exact value	lower bound	upper bound
Cm										
6	FOI	SST	C	U-T	1.40	7.91	1.00	-2.473	-2.473	-2.472
8	ARL	SST	U	U-T	1.35	2.46	0.98	-2.330	-2.404	-2.322
9	ARL	SST	U	U-T	1.41	5.21	0.90	-2.649	-2.779	-2.635
10	CORVID	SAR	U	U-T	1.50	6.07	0.98	-2.616	-2.628	-2.614
11	TÜBİTAK SAGE	k-e	U	U-T	1.36	4.89	0.96	-2.672	-2.743	-2.664
12	TÜBİTAK SAGE	SST	U	U-T	1.36	6.80	0.98	-3.084	-3.101	-3.082
13	TÜBİTAK SAGE	k-e	U	U-P	1.20	19.67	0.98	-2.426	-2.429	-2.426
14	TÜBİTAK SAGE	SST	U	U-P	1.20	28.29	1.02	-2.643	-2.643	-2.643
Cn										
4	MBDA F	SA-E	C	U-T	1.17	1.20	0.99	2.411	2.365	2.827
7	FOI	Laminar	C	U-T	1.40	13.13	0.99	2.792	2.792	2.792
10	CORVID	SAR	U	U-T	1.50	2.41	1.03	2.760	2.670	2.770
11	TÜBİTAK SAGE	k-e	U	U-T	1.36	3.54	1.01	2.717	2.681	2.721
18	DLR	SST	U	U-T	1.13	3.56	1.01	2.543	2.411	2.557

* Scheme → U: Upwind, C: Central; Mesh Type → S: Structured, O: Overset, U: Unstructured, T: Tetrahedral, P: Polyhedral

Acknowledgments

The authors would like to acknowledge the contributions made to this paper by their fellow AVT 316 Missile Faceteers: (in alphabetical order, by organisation) Kilian Cooley & Greg McGowan (Corvid Technologies), Henry Bucklow (ITI), Nigel Taylor (MBDA UK), and Michael A. Park (NASA Langley research Center). As befits a missile-related team, there have been no passengers in the pursuit of our objectives and our shared experience has provided a valuable backdrop for this paper.

References

[1] Kubin, J. S., An Analysis of Steady Asymmetric Vortex Shedding from a Missile at High Angles of Attack, Air Force Inst. of Tech. Wright-Patterson AFB, OH, 1973
[2] Deffenbaugh, F. D., Koerne, W. G., Asymmetric vortex wake development on missiles at high angles of attack, Journal of Spacecraft and Rockets, 1977
[3] Ericsson, L. E., Reding, J. P., Steady and unsteady vortex-induced asymmetric Loads on slender vehicles , Journal of Spacecraft and Rockets, 1982
[4] Hunt, B., Asymmetric vortex forces and wakes on slender bodies, 9th Atmospheric Flight Mechanics Conference, 1982
[5] Fidler, J. E., Bateman, M. C., Asymmetric vortex effects on missile configurations, Journal of Spacecraft and Rockets, 1975
[6] Keener, E. R., Chapman, G. T., Similarity in vortex asymmetries over slender bodies and wings, AIAA Journal, 1977
[7] Rom, J., High Angle of Attack Aerodynamics, New York: Springer-Verlag, 1992
[8] Bertin, J. J., Aerodynamics for Engineers, New Jersey: Prentice-Hall, 2002
[9] Cummings, R. M., Forsythe, J. R., Morton, S. A., Squires, K. D., Computational challenges in high angle of attack flow prediction, Progress in Aerospace Sciences, 2003
[10] Fidler, J. T., Approximate method for estimating wake vortex strength, AIAA Journal, 1974
[11] Taylor, N. et al., "The Prediction of Vortex Interactions on a Generic Missile Configuration Using CFD: Current Status of Activity in NATO AVT-316," NATO STO-MP-AVT-307, Paper 24, October 2019.
[12] Taylor, N., "AVT-316 Missile Facet: Overview of its Formation, Objectives and Manner of Working", paper to be presented at AIAA SciTech 2022, January 2022.
[13] Park, M.A., and DeSpirito, J., "The Influence of Adaptive Mesh Refinement on the Prediction of Vortex Interactions about a Generic Missile Airframe", paper to be presented at AIAA SciTech 2022, January 2022.
[14] Anderson, M et al., "The Influence of the Numerical Scheme in Predictions of Vortex Interaction about a Generic Missile Airframe", paper to be presented at AIAA SciTech 2022, January 2022.
[15] Shaw, S, et al., "The influence of modelling in predictions of vortex interactions about a generic missile airframe: RANS", paper to be presented at AIAA SciTech 2022, January 2022.

[16] Tormalm, M., et al., “The Influence of Scale Resolving Simulations in Predictions of Vortex Interaction about a Generic Missile Airframe”, paper to be presented at AIAA SciTech 2022, January 2022.
[17] Boychev, K., Barakos, G. and Steijl, R., “Simulations of flows around complex and simplified supersonic store geometries at high incidence angles using statistical and scale resolving turbulence models”, paper to be presented at AIAA SciTech 2022, January 2022.
[18] Loupy, G.J.M., “A Focused Study into the Prediction of Vortex Formation about Generic Missile and Combat Aircraft Airframes”, paper to be presented at AIAA SciTech 2022, January 2022.
[19] Schnepf, C., and Tormalm, M., “Comparisons of predicted and measured aerodynamic characteristics of the DLR LK6E2 missile airframe”, paper to be presented at AIAA SciTech 2022, January 2022.
[20] DeSpirito, J., et al., “Comparisons of Predicted and Measured Aerodynamic Characteristics of the DLR LK6E2 Missile Airframe (Scale Resolving)”, paper to be presented at AIAA SciTech 2022, January 2022.
[21] Taylor, N., “AVT-316 Missile Facet: 316 Missile Facet: Lessons learned concerning the prediction of Vortex Flow Interactions about Generic Missile Configurations”, paper to be presented at AIAA SciTech 2022, January 2022.
[22] “AVT-316: Vortex Interaction Effects Relevant to Military Air Vehicle Performance”, NATO STO-TR-AVT-316, to be published in 2022.
[23] Pointwise, Version 18, Pointwise, Inc., Fort Worth, TX, 2019.
[24] RavenCFD, Version 4.503, Corvid Technologies, Mooresville, NV, 2019
[25] CENTAUR, CENTAUR Software, https://www.centaursoft.com/
[26] Schwamborn, D., Gerhold, T. and Heinrich, R., “The DLR TAU-Code: Recent applications in research and industry”, Invited Lecture in “Proceedings on CD of the European Conference on Computational Fluid Dynamics ECCOMAS CFD 2006”, P. Wesseling, E. Oñate and J. Périaux (Eds), The Netherlands, 2006.
[27] ANSYS ICEM CFD Programmer’s Guide (Release 17.2), ANSYS Inc., 2016
[28] Tysell, L., “The TRITET Grid Generation System”. Proceedings of the 10th ISGG Conference on Numerical Grid Generation, Forth, Crete, Greece 2007.
[29] Eliasson, P., “Edge, a Navier-Stokes solver for unstructured grids”, Proc. To Finite Volumes for Complex Applications III, ISBN 1 9039 9634 1, pp.527-534, 2002.
[30] ANSA, Version 19.1.0, BETA CAE Systems, Switzerland, 2019.
[31] Pont, G., “Self adaptive turbulence models for unsteady compressible flows”, PhD Thesis, ENSAM, April 2015.
[32] Martineau, D.G., et al., “Anisotropic hybrid mesh generation for industrial RANS applications”, AIAA 2006-534, January 2006.
[33] ANSYS Meshing User's Guide (Release 15.0), ANSYS Inc., 2013.
[34] ANSYS Fluent Meshing (TGrid) User's Guide (Release 15.0), ANSYS Inc., 2013.
[35] ANSYS Fluent User's Guide (Release 14.0), ANSYS Inc., 2011.
[36] Lawson, S. and Barakos, G., “Review of Numerical Simulations For High-Speed, Turbulent Cavity Flows,” Progress in Aerospace Sciences, Vol. 47, No. 3, pp. 186 – 216, 2011.
[37] Mestreau, E. et al., CAPSTONE “CREATE-MG Capstone: Design, Architecture & Feature Modelling Improvements”, AIAA-2019-1716, January 2019.
[38] CFD++ Version 18.1 User Manual, Metacomp Technologies, Inc., Agoura Hills, CA, 2018.
[39] McDaniel, D. R. and Tuckey, T. R., “HPCMP CREATETM-AV Kestrel: New Capabilities and Future Directions,” AIAA-2019-0840, January 2019.
[40] Holleman, R., Fringer O. and Stacey M., “Numerical diffusion for flow-aligned unstructured grids with application to estuarine modeling”, International Journal for Numerical Methods in Fluids, 72.11 (2013): 1117-1145.
[41] Schäfer, M., Numerik im Maschinenbau, Springer-Verlag, 2013.
[42] Slater, J. W., “Examining Spatial (Grid) Convergence”, https://www.grc.nasa.gov/WWW/wind/valid/tutorial/spatconv.html
[43] Schwer, Leonard E. "Is your mesh refined enough? Estimating discretization error using GCI." 7th LS-DYNA Anwenderforum 1.1 (2008): 45-54.
[44] Roache, Patrick J. "Quantification of uncertainty in computational fluid dynamics." Annual review of fluid Mechanics 29.1 (1997): 123-160.
[45] Roache, Patrick J. "Perspective: a method for uniform reporting of grid refinement studies." (1994): 405-413.
[46] Roache, P. J., Verification and validation in computational science and engineering. vol. 895. Albuquerque, NM: Hermosa, 1998.